International Journal of Heat and Mass Transfer 67 (2013) 637–645

Contents lists available at ScienceDirect

International Journal of Heat and Mass Transfer

journal homepage: www.elsevier.com/locate/ijhmt

Thermophotovoltaic emitters based on a two-dimensional grating/thin-film nanostructure

Bo Zhao [a], Liping Wang [a,b], Yong Shuai [a,c], Zhuomin M. Zhang [a,*]

[a] George W. Woodruff School of Mechanical Engineering, Georgia Institute of Technology, Atlanta, GA, USA
[b] School for Engineering of Matter, Transport & Energy, Arizona State University, Tempe, AZ, USA
[c] School of Energy Science and Engineering, Harbin Institute of Technology, Harbin, People's Republic of China

ARTICLE INFO

Article history:
Received 28 February 2013
Received in revised form 1 July 2013
Accepted 19 August 2013

Keywords:
Magnetic polariton
Surface plasmon polariton
Thermophotovoltaic emitter

ABSTRACT

Thermophotovoltaic (TPV) devices can convert thermal radiation directly into electricity. To improve the efficiency of TPV systems, wavelength-selective emitters are designed to take thermal energy from various heat sources and then emit photons to the TPV cells. A two-dimensional grating/thin-film nanostructure is proposed as an efficient emitter, whose performance is enhanced by the excitations of both surface plasmon polaritons (SPPs) and magnetic polaritons (MPs). Rigorous coupled-wave analysis is used to predict the emittance as well as the electromagnetic field and current density distributions. The normal emittance of the proposed nanostructure is shown to be wavelength-selective and polarization-insensitive. The mechanisms of SPP and MP excitations in the nanostructure are elucidated for different polarizations. The current–density loop further confirms the existence of magnetic resonances. Furthermore, the effect of azimuthal and polar angles on the emittance spectra is also investigated, suggesting that the proposed structure has high emittance not only in the normal direction but also at large oblique angles.

1. Introduction

Thermophotovoltaic (TPV) systems convert thermal energy directly into electricity and hold promise in waste heat recovery, solar energy harvesting, and space applications [1–3]. A TPV system is environmentally-friendly and requires two key components: an emitter that gives out radiation by receiving thermal energy from various heating sources, and a TPV cell that can generate electricity by absorbing incident photons from the emitter. The main challenges for such a technique are low conversion efficiency and power generation. Near-field thermal radiation has been proposed for the enhancement of TPV power generation by bringing the emitter and receiver in close proximity [4,5]. However, there exist technological barriers for utilizing nanoscale TPV systems in the near future. To improve efficiency of TPV systems, a more appealing way is to use a selective TPV emitter, which emits photons in a certain spectral range that matches with a specific TPV cell, because only when the photon energies are higher than the bandgap of the semiconductor material used in the TPV cell, the absorbed radiant energy can produce electron–hole pairs and thus generate electricity [1,6]. On the other hand, if the photon energies are too high, the conversion efficiency becomes too low. Usually, the emitter radiates energies in a broad spectral region and much of the energies are at longer wavelength with insufficient photon energies to produce electron–hole pairs. While band-pass filters may be used to improve the overall efficiency, this method is cumbersome and overheating of the filter may become problematic [7–9]. Therefore, wavelength-selective emitter is crucial to improve the conversion efficiency and power generation of TPV systems [10,11].

Micro/nanostructures of wide profile diversity are able to tailor thermal radiation by utilizing different physical mechanisms. Not only one-dimensional (1D) gratings [12,13], V-groove gratings [14], and photonic crystals [15–17], but also various two-dimensional (2D) nano/microstructures have been investigated as promising selective TPV emitters. Heinzel et al. [18] manufactured 2D wavelength-selective emitters for the near-infrared spectral range, but the emittance exhibited directional dependence. Pralle et al. [19] fabricated 2D gold gratings that can emit over selected wavelengths in the mid-infrared. Similarly, Sai et al. [20–22] experimentally demonstrated the potentials of 2D concave tungsten surface gratings as TPV emitters whose emittance is enhanced by exciting cavity resonances. Chen and Tan [23] designed a 2D convex tungsten grating structures as TPV emitters. Multilayer nano/microstructures have also been proposed to control thermal radiation [24–32]. Recently, Wang and Zhang [33] used a 1D tungsten trilayer grating/thin-film nanostructure as a selective TPV emitter by taking advantage of magnetic polaritons (MPs), which are resonant responses based on the excitation of induced current loops in

* Corresponding author. Tel.: +1 404 385 4225; fax: +1 404 894 8496.
E-mail address: zhuomin.zhang@me.gatech.edu (Z.M. Zhang).

0017-9310/$ - see front matter © 2013 Elsevier Ltd. All rights reserved.
http://dx.doi.org/10.1016/j.ijheatmasstransfer.2013.08.047

Nomenclature

d	film thickness, m
E	electric field, V/m
H	magnetic field, A/m
h	grating height, m
i	$\sqrt{-1}$
J	current density, A/m^2
l	lateral dimension of the tungsten patches, m
M or N	highest diffraction order in the x or y direction
m or n	diffraction order in the x or y direction
n	refractive index
R	(directional-hemispherical) reflectance
r	reflection coefficient
T	(directional-hemispherical) transmittance
t	transmission coefficient; time, s
w	groove width, m

Greek symbols

α'_λ	directional (spectral) absorptance
ε	dielectric function
ε_0	permittivity of vacuum, F/m
ε'_λ	directional (spectral) emittance
θ	polar angle, deg
κ	extinction coefficient
Λ	grating period, m
λ	wavelength in vacuum, μm
σ	electrical conductivity, S/m
ϕ	azimuthal angle, deg
ψ	polarization angle, deg
ω	angular frequency, rad/s

Subscripts

I–IV	regions defined in Fig. 1(c)
inc	incidence
m or n	index of diffraction order in the x or y direction
p	p polarization or TM wave
s	s polarization or TE wave

the structure by incident electromagnetic waves [34–39]. The emittance can be enhanced in the desired spectral range by exciting MPs and surface plasmon polaritons (SPPs) [40–44].

An ideal TPV emitter should not only be wavelength-selective, but also desired to be polarization-insensitive so that high emittance for both transverse electric wave (TE wave or s polarization) and transverse magnetic wave (TM wave or p polarization) can be achieved. However, since only TM waves can excite MPs and SPPs in the 1D grating/thin-film configuration, application of the emitter is somewhat limited. In this paper, a 2D trilayer structure is proposed as a wavelength-selective and polarization-insensitive TPV emitter. The radiative properties are calculated by the rigorous coupled-wave analysis (RCWA). The effects of polarization and both the azimuthal and polar angles on emittance are investigated. The emittance can be enhanced in the wavelength range of 0.5 μm < λ < 2.0 μm by exciting MPs and SPPs. The mechanism of MP is further explored by examining the loop formed by the current density vectors. The SPP dispersion relations are explored for both TE and TM waves.

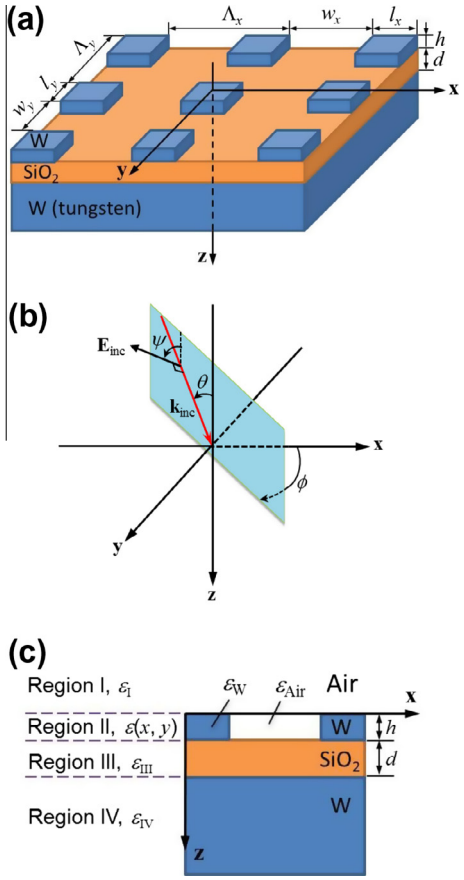

Fig. 1. Illustration of the numerical model for the 2D grating/thin-film nanostructure. The parameters used in the present study are $\Lambda_x = \Lambda_y = 600$ nm and $l_x = l_y = 300$ nm; thus $w_x = w_y = 300$ nm: (a) schematic of the structure; (b) the plane of incidence and polarization; (c) side view of the structure showing different regions and the dielectric functions.

2. Modeling and validation

2.1. Numerical method

Fig. 1(a) is a schematic of the 2D grating/thin-film structure considered in this work. The grating is made of rectangular tungsten (W) patches whose lateral dimensions are l_x and l_y with a height h and periods Λ_x and Λ_y. The periodic arrays of patches are on a thin dielectric film SiO_2 of thickness d that is deposited on a tungsten substrate. In the present study, the geometric parameters are fixed as follows: $\Lambda_x = \Lambda_y = 600$ nm, $l_x = l_y = 300$ nm, and $h = d = 60$ nm. The groove widths (i.e., the lateral distances between patches) are $w_x = w_y = 300$ nm. In order to predict the directional emittance (or emissivity), the indirect method is used here to calculate the directional-hemispherical reflectance (R) for light incident on the grating structure as indicated in Fig. 1(b). The incident radiation is assumed to be linearly polarized and can be characterized by the incident wavevector (with a polar angle θ and azimuthal angle ϕ) and polarization angle (ψ) with respect to the plane of incidence.

The incident plane wave is a propagating wave with a wavevector $\mathbf{k}_{inc} = (k_{x,inc}, k_{y,inc}, k_{z,inc})$ defined as follows:

$$k_{x,inc} = k_0 n_I \sin\theta\cos\phi,\ k_{y,inc} = k_0 n_I \sin\theta\sin\phi,\ \text{and}\ k_{z,inc} = k_0 n_I \cos\theta \tag{1}$$

where $k_0 = 2\pi/\lambda$ with λ being the wavelength in vacuum is the free-space wavevector. At normal incidence, only $\phi = 0$ needs to be considered. The polarization angle ψ characterizes the polarization

status and is defined as the angle between the electric field of the incident wave $\mathbf{E}_{inc}$ and the plane of incidence, i.e., the x–z plane. Therefore, $\psi = 0°$ and $\psi = 90°$ refer to TM and TE waves, respectively. Thus, the electric field of the incident wave at the origin and $t = 0$ can be expressed as

$$\mathbf{E}_{inc} = (\cos\psi\cos\theta\cos\phi - \sin\psi\sin\phi)\hat{\mathbf{x}} + (\cos\psi\cos\theta\sin\phi + \sin\psi\cos\phi)\hat{\mathbf{y}} - (\cos\psi\sin\theta)\hat{\mathbf{z}} \quad (2)$$

The electric field vector will oscillate according to $\mathbf{E}_{inc}\exp(ik_{x,inc}x + ik_{y,inc}y + ik_{z,inc}z - i\omega t)$, where ω is the angular frequency. In the calculation, the incident radiation can be set as either a TE wave ($\psi = 90°$) or a TM wave ($\psi = 0°$) because all other polarizations can be decomposed into these two polarizations. Since all the radiative properties concerned here are spectral properties, the word "spectral" is omitted in the description of the radiative properties. According to Kirchhoff's law [6], the directional emittance is equal to the directional absorptance, which is one minus the directional-hemispherical reflectance assuming that the bottom tungsten layer is opaque. Therefore, $\varepsilon'_\lambda = \alpha'_\lambda = 1 - R$ for either TE- or TM-wave incidence [33]. The problem becomes how to numerically calculate the reflectance of the emitter structure for any given wavelength, angle of incidence, and polarization status.

In the RCWA method, the space along the z-axis is divided into four regions, as illustrated by the side view shown in Fig. 1(c): Region I is the medium where radiation originates from, i.e., air or vacuum whose dielectric function $\varepsilon_I = (n_I + i\kappa_I)^2$ is taken as unity at all wavelengths; Region II is the grating layer and contains periodic nanostructures composed of free space and tungsten; and Regions III and IV consist of a SiO_2 spacer and a tungsten substrate, respectively. The optical properties of SiO_2 and tungsten, whose values are taken from [45], are wavelength dependent. Tungsten is chosen as the emitter material because it is corrosion resistant and can withstand high temperatures. For thin-film tungsten, the dielectric properties will somewhat deviate from those of the bulk materials [46]. In the present study, annealing and size effects on the tungsten properties are not considered.

A 2D RCWA algorithm is developed using MATLAB to numerically solve the Maxwell equations for determining the radiative properties of periodic structures. The diffraction orders are denoted as m and n in the x and y directions, respectively. The tangential component of the wavevector of each diffracted waves can be described by the Bloch-Floquet condition [6,47]:

$$k_{x,m} = k_{x,inc} + \frac{2\pi m}{\Lambda_x}, \quad k_{y,n} = k_{y,inc} + \frac{2\pi n}{\Lambda_y} \quad (3)$$

The z component of the wavevector of the reflected and transmitted electromagnetic waves with diffraction order (m, n) can be expressed as

$$k^r_{z,mn} = \begin{cases} \sqrt{k_I^2 - k_{x,m}^2 - k_{y,n}^2}, & k_I^2 \geqslant k_{x,m}^2 + k_{y,n}^2 \\ i\sqrt{k_{x,m}^2 + k_{y,n}^2 - k_I^2}, & k_I^2 < k_{x,m}^2 + k_{y,n}^2 \end{cases} \quad (4a)$$

or

$$k^t_{z,mn} = \begin{cases} \sqrt{k_{IV}^2 - k_{x,m}^2 - k_{y,n}^2}, & k_{IV}^2 \geqslant k_{x,m}^2 + k_{y,n}^2 \\ i\sqrt{k_{x,m}^2 + k_{y,n}^2 - k_{IV}^2}, & k_{IV}^2 < k_{x,m}^2 + k_{y,n}^2 \end{cases} \quad (4b)$$

where $k_I = k_0 n_I$ and $k_{IV} = k_0 n_{IV}$ are the wavevectors in the incident and substrate media. In this way, the electric and magnetic fields in each layer can be expressed as a superposition of the electromagnetic waves from all the diffraction orders, except in Region I where the incident wave should also be included. In addition, because of its periodicity, the dielectric function of the grating layer (Region II) can be expressed as a Fourier expansion. The tangential components of the electric and magnetic fields at the interface between two adjacent regions are continuous. A set of closed linear equations can be obtained by matching these boundary conditions, and then solved with matrix manipulations [48]. The diffraction efficiency for each order of the reflected and transmitted waves can be expressed as

$$DE_{R,mn} = |r_{s,mn}|^2 \mathrm{Re}\left(\frac{k^r_{z,mn}}{k_I\cos\theta}\right) + |r_{p,mn}|^2 \mathrm{Re}\left(\frac{k^r_{z,mn}}{k_I\cos\theta}\right) \quad (5a)$$

$$DE_{T,mn} = |t_{s,mn}|^2 \mathrm{Re}\left(\frac{k^t_{z,mn}}{k_I\cos\theta}\right) + |t_{p,mn}|^2 \mathrm{Re}\left(\frac{k^t_{z,mn}\varepsilon_I}{k_I\varepsilon_{IV}\cos\theta}\right) \quad (5b)$$

where r and t are the reflection and transmission coefficients, respectively, and subscripts p and s represent the components for TM and TE waves with respect to the output plane known as the plane of diffraction [49]. It should be noted that since the beam output plane is different from the plane of incidence, in general the polarization status of the diffracted waves will be different from the incident wave. The directional-hemispherical reflectance and transmittance can be obtained by summing up the diffraction efficiencies for all orders:

$$R = \sum DE_{R,mn} \text{ and } T = \sum DE_{T,mn} \quad (6)$$

In the present study, all the transmitted energy is absorbed by the tungsten substrate and the emittance is one minus the reflectance for given wavelength, incidence angle, and polarization. More detailed mathematical formulations for the 2D RCWA can be found in [23,48].

2.2. Validation of the numerical algorithm

The numerical accuracy of RCWA is dependent on the number of the diffraction orders and the Fourier expansion terms to synthesize the profile of the grating and they are related with each other. Referring M and N to the highest diffraction orders in the x and y directions, respectively, since $-M \leqslant m \leqslant +M$ and $-N \leqslant n \leqslant +N$, the total number of diffraction orders used in the calculation is $(2M + 1) \times (2N + 1)$ and the Fourier expansion terms will be $(4M + 1) \times (4N + 1)$ in total. Thus, one can simply investigate the effects of the number of diffraction orders on the accuracy. As more orders are used, the accuracy improves, however, both the memory required and the processing time consumed in the calculation increase dramatically. Thus, a convergence check was conducted to determine the number of diffraction orders needed to yield accurate results using reasonable computational time and resource. Fig. 2(a) shows the calculated normal emittance with different numbers of diffraction orders. In the calculation, M and N are set to be the same because same patterns are used along the x and y directions. It can be seen that, in the spectral region $0.3\ \mu m \leqslant \lambda \leqslant 2.0\ \mu m$, the emittance barely changes when the value of M is increased from 25 to 30. Hence, $M = 25$ is chosen in this region. However, for $2.0\ \mu m < \lambda \leqslant 3.0\ \mu m$, the calculated emittance is lower for $M = 40$ than $M = 30$, especially around $\lambda = 2.3\ \mu m$. The reflectance at $\lambda = 2.3\ \mu m$ is shown in Fig. 2(b) as a function of M to further study the numerical convergence. Since the wavelength is greater than twice of the period on either the x or y direction, for any angle of incidence, only the zero-order diffraction is propagating wave that contributes to the reflectance. The reflectance changes within 3% when M is increased from 35 to 50. The processing time scales with M to the sixth power (M^6), and it takes 140 min to calculate each single point for $M = 35$ using a dual eight core XEON E5-2687 W workstation. Hence, $M = 35$ is chosen in the calculation for $2.0\ \mu m < \lambda \leqslant 3.0\ \mu m$.

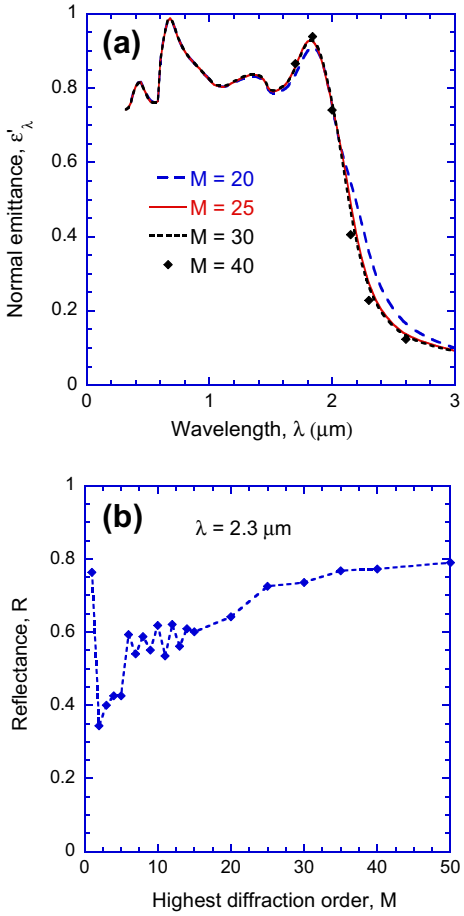

Fig. 2. Convergence test results: (a) normal emittance spectra calculated with different orders; (b) reflectance at $\lambda = 2.3$ μm calculated with different orders.

The emittance spectrum shown in Fig. 2(a) matches well with the $In_{0.2}Ga_{0.8}Sb$ p–n junction TPV cell, which has a bandgap λ_g around 2.1 μm [1]. As mentioned previously, a higher emittance at $\lambda < \lambda_g$ and lower emittance at $\lambda > \lambda_g$ is desired to improve the conversion efficiency. Since the TPV emitter temperature usually is less than 2000 K, the effect of emittance at wavelengths shorter than 0.5 μm on the conversion efficiency is much weaker according to Planck's blackbody spectral distribution. Therefore, it is desired to enhance the emittance in the wavelength region from 0.5 to 2.1 μm. The underlying mechanisms for the two highest emittance peaks, which elevate the whole emittance spectra, will be explored in the following section. The geometric parameters, such as the grating period and patch dimensions, can be adjusted to enhance emittance spectrum for use with other TPV cells with different bandgaps [1,50].

3. Results and discussion

3.1. The excitation of magnetic polaritons

Fig. 3 compares the normal emittance spectra calculated for the 2D structure shown in Fig. 1(a) and for the 1D grating/thin-film structure discussed in Ref. [33] for both TE and TM waves. The emittance spectrum for plain tungsten is also shown to help explain some of the peaks observed in the nanostructures. Note that the normal emittance is independent of polarization for the 2D structure. The emittance spectrum of the 1D grating/thin-film

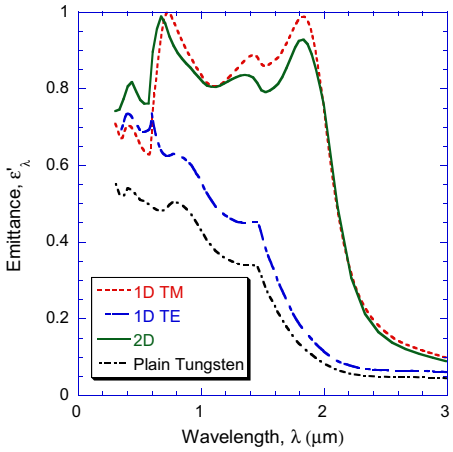

Fig. 3. Normal emittance spectra of the 2D structure and a 1D structure for both TE and TM waves, along with that of plain tungsten.

structure for TE waves is similar to that of plain tungsten except for the peak at 0.6 μm, which is due to Wood's anomaly [23,47]. Several small peaks located near 0.4, 0.6, and 1.4 μm are associated with the interband transitions of tungsten [45,46]. The peak near 0.6 μm does not appear in the spectra for the 2D structure or the 1D structure with TM waves. The emittance spectrum for the 1D structure with TM waves and that for the 2D structures are very similar, both contain two major emission peaks (near 0.7 and 1.8 μm) that do not exist in the spectra for the TE wave or plain tungsten. The overall emittance at normal direction is the average of those for TE and TM waves. As an example, the normal emittance $\lambda = 1.7$ μm for the 2D structure is 0.85 and the emittance averaged over the two polarizations for the 1D structure is only 0.58. Therefore, the throughput and efficiency of the TPV system can be significantly improved with the 2D grating/thin-film structure. The mechanisms responsible for the dominant emission peaks are discussed below.

The emittance peaks at $\lambda = 1.83$ μm is due to the coupling of the magnetic resonance inside a micro/nanostructure with the external electromagnetic waves or magnetic plasmon polariton. When the MP is excited, the magnetic field is strongly enhanced in the dielectric layer inserted between the tungsten grating and tungsten substrate, as shown in Fig. 4. The electric field and current density vectors, denoted by the arrows, are the instantaneous values at $t = 0$, while the magnetic field, represented by the color contour, is the square of relative amplitude. The maximum value of $|H_y/H_{inc}|^2$ in Fig. 4 is 26.0 as compared to 25.8 for the 1D structure (not shown here), suggesting that the magnitude of enhancement is about the same in both 1D and 2D structures. Also, the coupling between the metal patch and the substrate becomes weaker and the enhancement decreases as the slide parallel to the x–z plane is moved towards the patch edges. The emittance peak is higher for the 1D structure (TM waves) than for the 2D structure. It is interesting to note that even though the area under the tungsten grating for the 2D structure is only half of that for the 1D structure, the emittance can still be significantly enhanced with a peak near 0.93 when MP is excited.

An inductor–capacitor (LC) model, where the dielectric is regarded as a capacitor and the metal is treated as an inductor, was used by Wang and Zhang [33] to predict the MP resonance frequency. Since the resistance elements will not affect the resonance frequency, they are usually neglected for simplicity. The 2D structure has the same cross section as the 1D structure in the x–z plane. The same LC model can be used to predict the MP resonance frequency for the 2D structure, because the length in the y direction merely cancels out. The MP resonance wavelength can be ob-

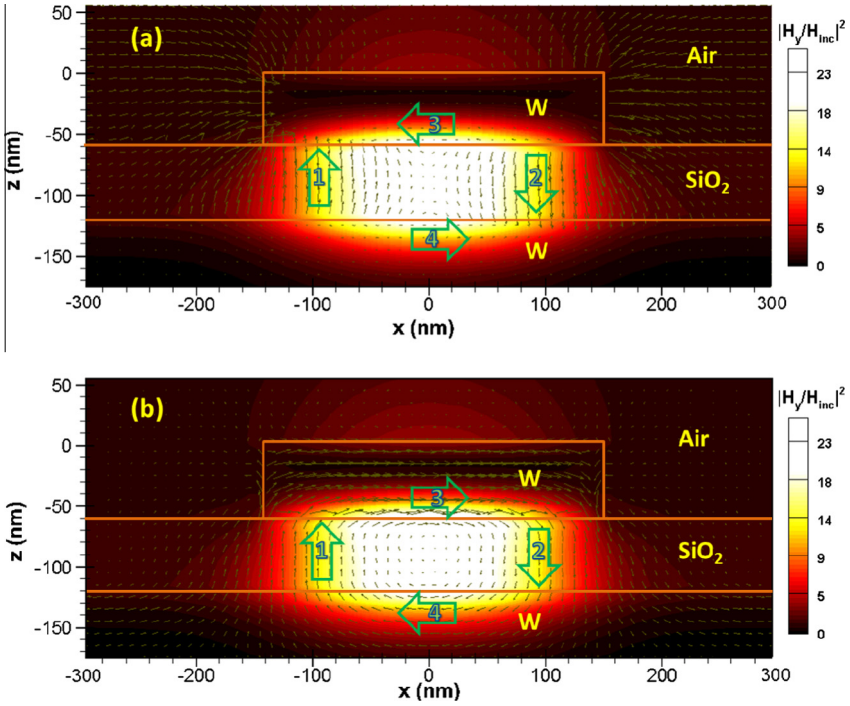

Fig. 4. The electromagnetic fields and current density distribution in the 2D structure for TM waves at normal incidence and $\lambda = 1.83$ μm. The fields are calculated at $y = 0$ in the x–z plane. The color shows the relative magnitude of the y component of the magnetic field. The vectors show the direction and magnitude of (a) the electric field and (b) current density. Note that $M = N = 40$ was used in the calculation.

tained to be 1.87 μm by zeroing the impedance of the circuit, which is in good agreement with the RCWA calculation. The electric field vectors were used to illustrate the antiparallel currents in the metal above and below the dielectric spacer [33,51]. However, the electric field vectors do not form a closed loop [52]. As shown in Fig. 4(a), the directions of the electric fields in the metal and dielectric layer are against each other. According to Lenz's law, the induced current should form a loop that will create a diamagnetism effect. In the following, the local current density vector is analyzed to illustrate that a current indeed forms a loop.

The electrical conductivity of a material is frequency dependent and is related to the dielectric function as [6]

$$\sigma = \sigma' + i\sigma'' = -i\omega\varepsilon\varepsilon_0 \tag{7}$$

where σ' and σ'' are the real and imaginary parts of the conductivity, ω is the angular frequency, and ε_0 is the vacuum permittivity. The current density vector is related to the electric field vector by $\mathbf{J} = \sigma\mathbf{E}$. Note that complex vector variables are used in the RCWA computational algorithm. However, only Re($\mathbf{E}$) represents the actual electric field. Similarly, only Re($\mathbf{J}$) represents the actual current density, which can be expressed as the sum of the conduction current and displacement current. Therefore,

$$\mathrm{Re}(\mathbf{J}) = \mathbf{J}_{\mathrm{cond}} + \mathbf{J}_{\mathrm{disp}} = \sigma'\mathrm{Re}(\mathbf{E}) - \sigma''\mathrm{Im}(\mathbf{E}) \tag{8}$$

The sign of the current density depends on the relative magnitude of these two terms. Fig. 4(b) shows the current density vectors Re($\mathbf{J}$), which do form a closed loop, in a unit cell of the 2D nanostructure. While the induced current always forms a closed loop, the directions of the current flow and electric field may or may not be the same.

The electric fields and current densities at four locations are calculated to illustrate how their signs vary in the metal and dielectric regions in the particular case studied here. The results are shown in Table 1, where locations 1 and 2 are on the left and right, respectively, of the dielectric layer and locations 3 and 4 are in the metal grating and substrate, respectively. For locations 1 and 2, $|\sigma''| \gg \sigma'$ and displacement current is the dominant contribution to the current density. Since σ'' is negative, $\mathbf{J}_{\mathrm{disp}}$ will be in the same direction as the imaginary part of $\mathbf{E}$. Additionally, the x component of $\mathbf{E}$ is negligibly small in these locations. Because the real and imaginary parts of E_z have the same sign, it can be inferred that the displacement current is in the same direction as the electric field. For locations 3 and 4, the electric field is almost parallel to x and only E_x needs to be considered. For tungsten at this wavelength, σ' and σ'' are both positive and on the same order of magnitude. From the RCWA calculation, the real and imaginary parts of E_x share the same sign. According to Eq. (8), the conduction and displacement current densities must have opposite signs. Since the magnitude of the displacement current density is greater than the conduction current density, the full current density follows the direction of the displacement current density, which is opposite to the electric field in the x direction. In general, the real and imaginary parts of the electric field may not have the same sign. Thus, it is possible for the current density and electric field in the dielectric layer to have different signs. Similarly, depending on the signs of the electric field and conductivity, the current density and electric field in the metal region can have the same or different signs. Nevertheless, the current flow always forms a closed loop. Since the instantaneous electric field vectors in Fig. 4 will oscillate with time, the direction of the arrows may reverse but should always be antiparallel.

Fig. 5 shows the emittance spectra of the 2D structure at different polar angles for both TM and TE waves for $\phi = 0°$. It can be seen that the location of the emittance peak near 1.83 μm changes little with θ for both TE and TM waves, because the resonance frequency of MPs only depends on the geometric structure and materials involved. For TE waves, MPs are excited by the x component of the magnetic field. The patterns are the same in both the x and y directions; thus, it is expected that the MP resonance frequency does

Table 1
Numerical values of the electric field and current density at $t = 0$ for the four locations on Fig. 4. For locations 1 and 2, the z components of the current density and electric field vectors are given; while for locations 3 and 4, their x components are given.

Location	x (nm)	z (nm)	Re(E) (V/m)	Im(E) (V/m)	σ' (S/m)	σ'' (S/m)	J_{cond} (A/m^2)	J_{disp} (A/m^2)	Re(J) (A/m^2)
1	−95	−85	3.07	2.42	0.123	-1.89×10^4	0.379	4.57×10^4	4.57×10^4
2	95	−85	−3.07	−2.42	0.123	-1.89×10^4	−0.379	-4.57×10^4	-4.57×10^4
3	5	−45	−0.241	−0.808	1.79×10^5	3.63×10^5	-4.32×10^4	2.93×10^5	2.50×10^5
4	5	−135	0.388	0.362	1.79×10^5	3.63×10^5	6.94×10^4	-1.32×10^5	-6.23×10^4

not change. Furthermore, the peak emittance remains nearly the same even though θ is increased to 60° for TM waves similar to what has been observed previously for 1D structure [33–35]. For TE waves, however, since the x component of the magnetic field is decreasing as θ increases, the field enhancement becomes weaker at larger polar angles. Hence, the emittance peak associated with the MP decreases as θ increases, as shown in Fig. 5(b). The location of the emittance peak near $\lambda = 0.7$ μm at $\phi = 0°$ shifts in wavelength as θ changes. The underlying mechanisms are elucidated in the next section by considering the excitation of SPPs in the nanostructure.

3.2. The excitation of surface plasmon polaritons

The emittance peak around $\lambda = 0.7$ μm of the 2D structure emittance spectrum on Fig. 3 is because of the excitation of SPPs. Plasmons are quasi-particles associated with oscillations of plasma, which is a collection of charged particles in metal. The strong coupling of external electromagnetic waves with surface plasma is called an SPP, which results in a surface wave propagating along the interface between the dielectric and the metal. Because of the non-radiative nature of the SPPs, the wavevector of surface plasmon is always larger than the free space wavevector [53]. For two bulk nonmagnetic materials, the magnitude of the wavevector of the surface plasmon can be expressed as

$$|\mathbf{k}_{SP}| = \frac{\omega}{c_0}\sqrt{\frac{\varepsilon_1\varepsilon_2}{\varepsilon_1+\varepsilon_2}} \tag{9}$$

where c_0 is the speed of light in vacuum, and ε_1 and ε_2 are the dielectric functions of the dielectric and metal, respectively, and their real parts are of opposite signs. Eq. (9) involves complex values of the dielectric functions and the solution will result in complex wavevectors for real frequencies. For this work, only the real parts of $\varepsilon_1(\omega)$ and $\varepsilon_2(\omega)$ are considered as typically done in analyzing SPPs [6,54]. To excite SPPs, the electromagnetic waves (which include both the incident wave and the diffracted waves) must have a tangential component equal to $\mathbf{k}_{SP}$. Furthermore, when SPPs are excited, the surface current density associated with the surface plasmon in the material must have a component parallel to $\mathbf{k}_{SP}$, which means that the electric field of the electromagnetic waves should have a component parallel to $\mathbf{k}_{SP}$ as well [55]. For a 1D grating whose grooves are parallel to the y axis, only TM waves can excite SPPs when the plane of incidence is in the x–z plane [48,53]. However, for conical incidence or for 2D gratings, both TE and TM waves can excite SPPs [55,56], and SPPs may propagate along either the x or y direction.

Following the Bloch–Floquet condition shown in Eq. (3), the tangential component of the wavevector of the (m, n) order of the diffracted waves can be expressed as

$$\mathbf{k}_{\parallel,mn} = \left(k_{x,\mathrm{inc}} + \frac{2\pi m}{\Lambda_x}\right)\hat{\mathbf{x}} + \left(k_{y,\mathrm{inc}} + \frac{2\pi n}{\Lambda_y}\right)\hat{\mathbf{y}} \tag{10}$$

where the subscript ∥ denotes the component in the x–y plane. As shown in Fig. 5(a), the emittance peak due to SPP excitation shifts toward longer wavelength as the polar angle increases for TM waves. For TE waves as shown in Fig. 5(b), the peak location shifts toward shorter wavelengths with increasing polar angles. The mechanisms can be understood by studying the behaviors of SPPs for both TM and TE waves in the 2D structure as discussed below.

Fig. 6(a) shows the contour plot of the emittance for the 2D structure at TM waves in terms of wavenumber and the x component of the free-space wavevector, calculated by the 2D RCWA. The oblique bright bands indicate the emittance enhancement due to SPPs, while the flat bright band around 5400 cm^{-1} is due to the excitation of MP as discussed previously. It can be seen that SPPs have a strong directional dependence, but the MP resonance frequency is insensitive to the polar angle since $k_x = k_0 \sin\theta$. Besides, the branch with $m = 0$ and $n = 0$ cannot excite SPPs since it is always beyond (while very close to) the light line. The lower-right corner beyond the light line is simply left blank.

The contour plots are calculated with $M = N = 15$ here with the 2D RCWA to save the computation time. The results are sufficiently accurate at wavenumbers higher than approximately 7000 cm^{-1}, which is the major region of interest for SPPs. Rela-

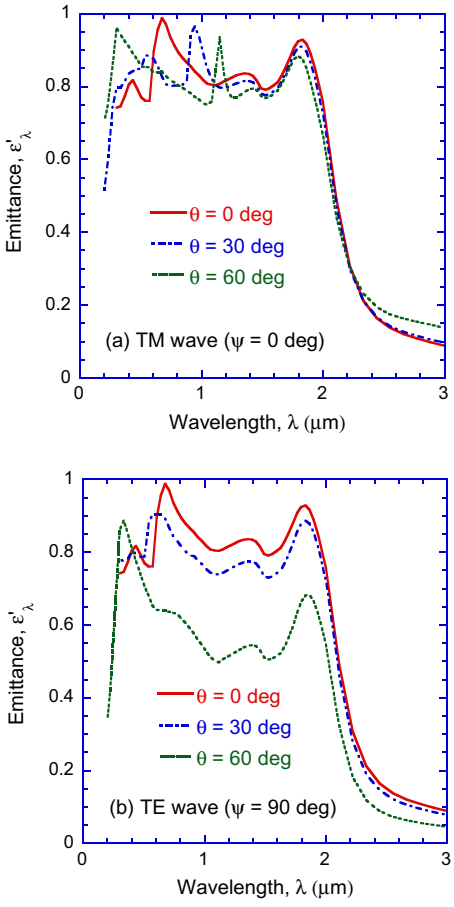

Fig. 5. Emittance spectra of the 2D structure at different polar angles for: (a) TM waves; (b) TE waves.

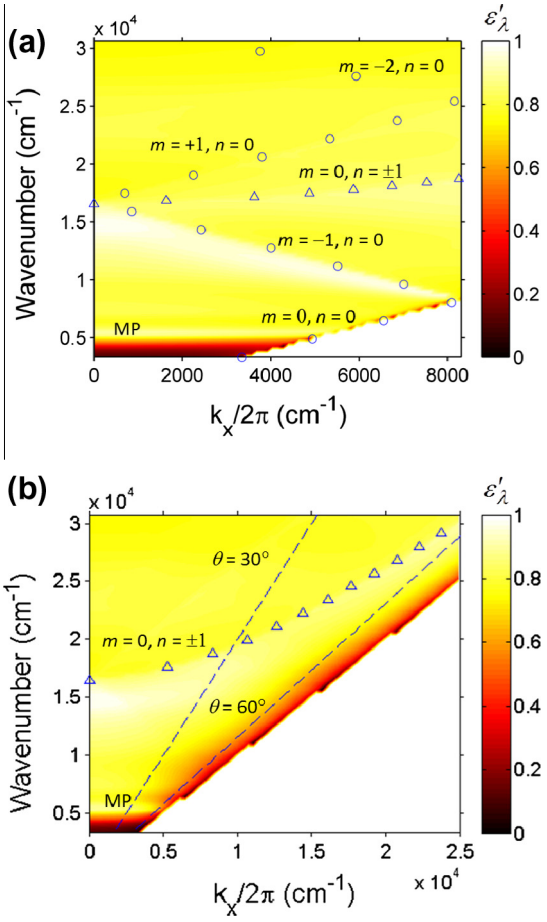

Fig. 6. Emittance contour plots of the 2D grating/thin-film structure from RCWA calculations along with the SPP dispersion relations: (a) TM waves; (b) TE waves.

tively larger errors (but still within 5%) exist at wavenumbers below 7000 cm^{-1} when compared to the results calculated with $M = N = 25$ at normal incidence. Finite-difference time-domain (FDTD) method is also used to verify the contour plots obtained from the 2D RCWA at $\theta \leqslant 60^\circ$. The results compare well with each other. At polar angles exceeding 60°, the computational time required for the FDTD to calculate the emittance spectra increases significantly. Thus, RCWA with fewer orders should be considered to be both reasonable and practical for generating the contour plots.

A 2D grating surface structure has periodicity in both the x and y directions. For TM polarized incident waves, the tangential component of the electric field of the incident wave has a zero y component, i.e., $k_{y,\mathrm{inc}} = 0$ since $\phi = 0^\circ$. The effect of the periodicity in the x direction can be analyzed by assuming $n = 0$ in Eq. (10). In this case, SPPs can be excited along the x direction once the following dispersion relation is satisfied:

$$\frac{\omega}{c_0}\sqrt{\frac{\varepsilon_1\varepsilon_2}{\varepsilon_1+\varepsilon_2}} = \left|k_0 \sin\theta + \frac{2\pi m}{\Lambda_x}\right| \tag{11}$$

This dispersion relation is solved with different m values (−2, −1, 0, and +1) for SPPs excited between air and tungsten, and the resonance frequencies are marked as circles in Fig. 6(a). These circles follow well the bright emittance band obtained from the 2D RCWA calculation. The emittance band associated with the $m = -1$ order is broader and the resonance frequencies predicted by the dispersion relation given in Eq. (11) are slightly higher than those from RCWA. This is mainly caused by the existence of the SiO_2 layer, which could affect the SPP frequency since the SPPs on W-SiO_2 interface predicted by Eq. (11) are lower than the RCWA results. It is difficult to accurately predict the SPP locations when a thin dielectric film is involved. Furthermore, losses in tungsten can broaden the emittance peak, which has been verified by using a simple 1D tungsten grating without SiO_2 film, although the results are not shown here.

For 2D periodic grating structures, the periodicity (Λ_y) in the y direction can affect SPP dispersion as well according to Eq. (10). Take $m = 0$ and $n \neq 0$ for simplicity. The incident wave will be diffracted into the y direction. The electric field of the reflected waves will have a component along the y axis even though the incident wave does not carry an electric filed in the y direction. When $m = 0$, the SPP dispersion relation becomes

$$\frac{\omega}{c_0}\sqrt{\frac{\varepsilon_1\varepsilon_2}{\varepsilon_1+\varepsilon_2}} = \sqrt{(k_0 \sin\theta)^2 + \left(\frac{2\pi n}{\Lambda_y}\right)^2} \tag{12}$$

The solutions of this equation are marked on Fig. 6(a) with triangles and they agree well with the emittance band obtained from the 2D RCWA. Within the considered ranges of frequency and wavevector, only the SPP associated with $n = \pm 1$ shows up when $m = 0$. This branch will fold with the grating period Λ_x in the x direction and show up as $m = \pm 1, \pm 2$ orders. However, these higher orders also do not show up in the contour plot due to the intrinsic losses of tungsten. At wavelengths shorter than the grating period of 0.6 μm, the peaks shown in Fig. 6(a) become complicated because higher-order SPPs, Wood's anomaly, and higher-order MPs can couple with each other [57]. Moreover, losses in tungsten can also increase the emittance as well as bandwidth, making it difficult to identify the peak locations at short wavelengths.

For TE incident waves, the periodicity in the y direction plays a crucial role to excite SPPs. Fig. 6(b) shows the emittance contour of the 2D structure for TE waves, calculated with RCWA. The plot is extended beyond the first Brillouin zone (i.e., $k_x > \pi/\Lambda$) and lines with polar angles $\theta = 30^\circ$ and 60° are identified. Again, the lower-right region beyond the light line is left blank. The dispersion relation can be solved by combining Eqs. (9) and (10). However, for TE wave incidence with $\phi = 0^\circ$, the order n must not be zero since k_y must have a nonzero real part for SPPs to propagate in the y direction. As can be seen from Fig. 6(b), besides the flat MP resonance band in the low frequency region, a bright resonance band is also observed whose resonance frequency increases with k_x. This branch is identified as the SPP dispersion with $m = 0$ and $n = \pm 1$ and can be calculated from Eq. (12) as shown by the triangles. The actual dispersion predicted by RCWA is somewhat lower and broader due to the existence of the SiO_2 film and loss in tungsten as discussed previously. Higher-order SPP branches can also be predicted by Eq. (10) but cannot be discerned from the contour plot. Moreover, Wood's anomaly may exist especially for the $m = 1$ and $n = 0$ order, although it is not clearly shown in Fig. 6(b). The trend that the SPP excitation wavelength decreases with increasing polar angle agrees with that shown in Fig. 5(b) for the 2D structure.

3.3. The effect of polar angle and azimuthal angle

The effect of the polar angle and azimuthal angle on the emittance of the 2D structure is also investigated at $\lambda = 0.5$, 1.0, 1.6, 1.8 and 2.2 μm. The first four wavelengths fall in the wavelength range for TPV cells that high emittance is desirable. However, low emittance is desired at $\lambda = 2.2$ μm and beyond. Fig. 7 is a polar plot of the emittance with respect to θ at the azimuthal angle $\phi = 0^\circ$. The left and right sides of the plot show the emittance for TM and TE waves, respectively, since θ can only vary from 0° to 90°. This plot is also valid for $\phi = 90^\circ$, 180°, or 270°, due to the symmetry of the structure. The emittance is above 0.7 for polar angles less than 40° for both TM and TE waves in the desired wave-

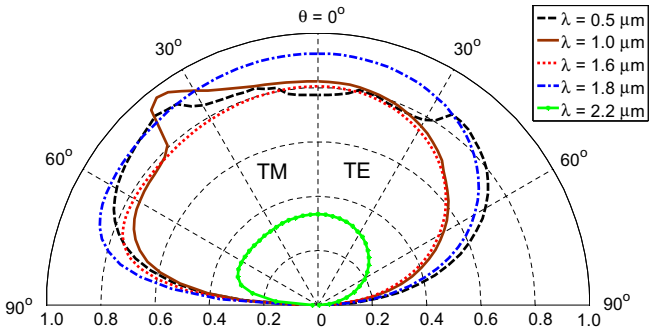

Fig. 7. Polar plots of the emittance at $\phi = 0°$, 90°, 180° or 270° for several given wavelengths. The left half is for TM waves and the right half is for TE waves.

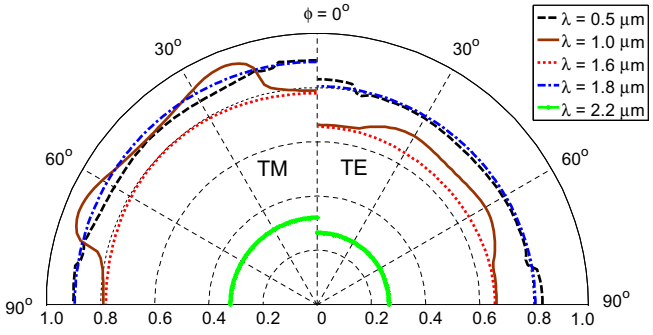

Fig. 8. Polar plots of emittance at $\theta = 45°$ for several given wavelengths. The left half is for TM waves and the right half is for TE waves. Only the results for $0° \leqslant \phi \leqslant 90°$ is shown since the emittance has an eightfold symmetry with respect to ϕ.

length range. For $\lambda = 2.2$ μm, the maximum emittance is about 0.3, which will further decrease at longer wavelengths. Based on the previous analysis, the emittance peak around $\theta = 38°$ at $\lambda = 1$ μm for TM waves and that around $\theta = 35°$ at $\lambda = 0.5$ μm for TE waves are due to the excitation of SPPs. The MP excitation results in high emittance at $\lambda = 1.8$ μm for a large range of polar angles, especially for TM waves.

The effect of ϕ on the emittance is studied by fixing $\theta = 45°$, and the results are shown in Fig. 8. The azimuthal angle ϕ can vary from 0° to 360°. However, due to the symmetry of the 2D structure, the emittance polar plots for both TE and TM waves have an eightfold symmetry. Hence, only the emittance for $0° < \phi < 90°$ is shown. Again, the left side displays the emittance for TM waves ($\psi = 0°$) and the right side displays the emittance for TE waves ($\psi = 90°$). For the wavelengths in the desired range, the emittance is higher than 0.78 and 0.64 for TM and TE waves, respectively. For $\lambda = 2.2$ μm, the emittance is lower than 0.35 for both polarizations at all azimuthal angles, which again shows the wavelength selectivity and angle independence of the emittance of the nanostructure. As mentioned previously, the geometric parameters can be tuned to fit TPV cell materials with different bandgaps. As Eqs. (11) and (12) suggest, SPPs only depend on the grating period. For MP resonances, a larger lateral dimension of patches will result in the red shift of the emittance peak. Also, increasing the thickness of the dielectric layer will decrease the MP resonance wavelength. These properties can be used in the design of practical TPV emitters once the TPV cell materials and properties are known.

4. Conclusions

This work theoretically demonstrates the advantages of using a 2D periodic array of tungsten patches over a thin dielectric film coated on a tungsten substrate as a high-performance TPV emitter. The normal emittance of this 2D nanostructure is wavelength-selective and polarization-independent. Furthermore, the mechanisms of excitation of MPs and SPPs in the 2D structure are elucidated. The two peaks in the emittance spectra are explained by the excitation of SPPs and MPs. The current density vectors are analyzed to show that when MP is excited, the induced current indeed forms a loop. Furthermore, it is shown that high emittance can be achieved in the desired spectral region for both polarizations with the 2D nanostructure in a large range of polar and azimuthal angles. The detailed analysis and findings from this study not only will help understand the mechanisms that can be used to tailor the emittance for the proposed 2D structure, but also will facilitate the design and optimization for plasmonic nanostructures for applications in TPV systems and solar cells.

Acknowledgements

This work was mainly supported by the US Department of Energy (DE-FG02-06ER46343). LPW would like to thank the Startup Program at the Arizona State University. YS would like to thank the National Natural Science Foundation of China (No. 50930007). The authors would like to thank Dr. Atsushi Sakurai for the help in the FDTD simulation.

References

[1] S. Basu, Y.-B. Chen, Z.M. Zhang, Microscale radiation in thermophotovoltaic devices—a review, Int. J. Energy Res. 31 (2007) 689–716.
[2] T.J. Coutts, A review of progress in thermophotovoltaic generation of electricity, Renewable Sustainable Energy Rev. 3 (1999) 77–184.
[3] V.L. Teofilo, P. Choong, J. Chang, Y.L. Tseng, S. Ermer, Thermophotovoltaic energy conversion for space, J. Phys. Chem. C 112 (2008) 7841–7845.
[4] K. Park, S. Basu, W.P. King, Z.M. Zhang, Performance analysis of near-field thermophotovoltaic devices considering absorption distribution, J. Quant. Spectrosc. Radiat. Transfer 109 (2008) 305–316.
[5] M. Francoeur, R. Vaillon, M.P. Mengüç, Thermal impacts on the performance of nanoscale-gap thermophotovoltaic power generators, IEEE Trans. Energy Convers. 26 (2011) 686–698.
[6] Z.M. Zhang, Nano/Microscale Heat Transfer, McGraw-Hill, New York, 2007.
[7] L. Mao, H. Ye, New development of one-dimensional Si/SiO_2 photonic crystals filter for thermophotovoltaic applications, Renewable Energy 35 (2010) 249–256.
[8] R.T. Kristensen, J.F. Beausang, D.M. DePoy, Frequency selective surfaces as near-infrared electromagnetic filters for thermophotovoltaic spectral control, J. Appl. Phys. 95 (2004) 4845–4851.
[9] T. Bauer, I. Forbes, N. Penlington, N. Pearsall, Heat transfer modelling in thermophotovoltaic cavities using glass media, Sol. Energy Mater. Sol. Cells 88 (2005) 257–268.
[10] J. Baxter, Z. Bian, G. Chen, D. Danielson, M.S. Dresselhaus, A.G. Fedorov, T.S. Fisher, C.W. Jones, E. Maginn, U. Kortshagen, A. Manthiram, A. Nozik, D.R. Rolison, T. Sands, L. Shi, D. Sholl, Y. Wu, Nanoscale design to enable the revolution in renewable energy, Energy Environ. Sci. 2 (2009) 559–588.
[11] P. Bermel, M. Ghebrebrhan, W. Chan, Y.X. Yeng, M. Araghchini, R. Hamam, C.H. Marton, K.F. Jensen, M. Soljačić, J.D. Joannopoulos, S.G. Johnson, I. Celanovic, Design and global optimization of high-efficiency thermophotovoltaic systems, Opt. Express 18 (2010) A314–A334.
[12] N. Nguyen-Huu, Y.-B. Chen, Y.-L. Lo, Development of a polarization-insensitive thermophotovoltaic emitter with a binary grating, Opt. Express 20 (2012) 5882–5890.
[13] Y.-B. Chen, Z.M. Zhang, Design of tungsten complex gratings for thermophotovoltaic radiators, Opt. Commun. 269 (2007) 411–417.
[14] N.P. Sergeant, M. Agrawal, P. Peumans, High performance solar-selective absorbers using coated sub-wavelength gratings, Opt. Express 18 (2010) 5525–5540.
[15] P. Nagpal, S.E. Han, A. Stein, D.J. Norris, Efficient low-temperature thermophotovoltaic emitters from metallic photonic crystals, Nano Lett. 8 (2008) 3238–3243.
[16] A. Narayanaswamy, G. Chen, Thermal emission control with one-dimensional metallodielectric photonic crystals, Phys. Rev. B 70 (2004) 125101.
[17] J.H. Lee, Y.S. Kim, K. Constant, K.M. Ho, Woodpile metallic photonic crystals fabricated by using soft lithography for tailored thermal emission, Adv. Mater. 19 (2007) 791–794.
[18] A. Heinzel, V. Boerner, A. Gombert, B. Bläsi, V. Wittwer, J. Luther, Radiation filters and emitters for the NIR based on periodically structured metal surfaces, J. Mod. Opt. 47 (2000) 2399–2419.
[19] M.U. Pralle, N. Moelders, M.P. McNeal, I. Puscasu, A.C. Greenwald, J.T. Daly, E.A. Johnson, T. George, D.S. Choi, I. El-Kady, R. Biswas, Photonic crystal enhanced narrow-band infrared emitters, Appl. Phys. Lett. 81 (2002) 4685–4687.

[20] H. Sai, H. Yugami, Thermophotovoltaic generation with selective radiators based on tungsten surface gratings, Appl. Phys. Lett. 85 (2004) 3399–3401.
[21] H. Sai, Y. Kanamori, H. Yugami, High-temperature resistive surface grating for spectral control of thermal radiation, Appl. Phys. Lett. 82 (2003) 1685–1687.
[22] H. Sai, Y. Kanamori, H. Yugami, Tuning of the thermal radiation spectrum in the near-infrared region by metallic surface microstructures, J. Micromech. Microeng. 15 (2005) S243.
[23] Y.-B. Chen, K.H. Tan, The profile optimization of periodic nano-structures for wavelength-selective thermophotovoltaic emitters, Int. J. Heat Mass Transfer 53 (2010) 5542–5551.
[24] P. Bouchon, C. Koechlin, F. Pardo, R. Haïdar, J.-L. Pelouard, Wideband omnidirectional infrared absorber with a patchwork of plasmonic nanoantennas, Opt. Lett. 37 (2012) 1038–1040.
[25] C.-M. Wang, Y.-C. Chang, M.-W. Tsai, Y.-H. Ye, C.-Y. Chen, Y.-W. Jiang, Y.-T. Chang, S.-C. Lee, D.P. Tsai, Reflection and emission properties of an infrared emitter, Opt. Express 15 (2007) 14673–14678.
[26] Y. Cui, J. Xu, K.H. Fung, Y. Jin, A. Kumar, S. He, N.X. Fang, A thin film broadband absorber based on multi-sized nanoantennas, Appl. Phys. Lett. 99 (2011) 253101.
[27] J. Hendrickson, J. Guo, B. Zhang, W. Buchwald, R. Soref, Wideband perfect light absorber at midwave infrared using multiplexed metal structures, Opt. Lett. 37 (2012) 371–373.
[28] G. Lévêque, O.J.F. Martin, Tunable composite nanoparticle for plasmonics, Opt. Lett. 31 (2006) 2750–2752.
[29] X. Liu, T. Tyler, T. Starr, A.F. Starr, N.M. Jokerst, W.J. Padilla, Taming the blackbody with infrared metamaterials as selective thermal emitters, Phys. Rev. Lett. 107 (2011) 045901.
[30] N. Liu, M. Mesch, T. Weiss, M. Hentschel, H. Giessen, Infrared perfect absorber and its application as plasmonic sensor, Nano Lett. 10 (2010) 2342–2348.
[31] I. Puscasu, W.L. Schaich, Narrow-band, tunable infrared emission from arrays of microstrip patches, Appl. Phys. Lett. 92 (2008) 233102–233103.
[32] J. Wang, C. Fan, P. Ding, J. He, Y. Cheng, W. Hu, G. Cai, E. Liang, Q. Xue, Tunable broad-band perfect absorber by exciting of multiple plasmon resonances at optical frequency, Opt. Express 20 (2012) 14871–14878.
[33] L.P. Wang, Z.M. Zhang, Wavelength-selective and diffuse emitter enhanced by magnetic polaritons for thermophotovoltaics, Appl. Phys. Lett. 100 (2012) 063902.
[34] L.P. Wang, Z.M. Zhang, Measurement of coherent thermal emission by exciting magnetic polaritons in subwavelength grating structure, J. Heat Transfer (2012).
[35] B.J. Lee, L.P. Wang, Z.M. Zhang, Coherent thermal emission by excitation of magnetic polaritons between periodic strips and a metallic film, Opt. Express 16 (2008) 11328–11336.
[36] L.P. Wang, Z.M. Zhang, Resonance transmission or absorption in deep gratings explained by magnetic polaritons, Appl. Phys. Lett. 95 (2009) 111904.
[37] N. Dahan, A. Niv, G. Biener, Y. Gorodetski, V. Kleiner, E. Hasman, Extraordinary coherent thermal emission from SiC due to coupled resonant cavities, J. Heat Transfer 130 (2008) 112401.
[38] H. Liu, T. Li, Q.J. Wang, Z.H. Zhu, S.M. Wang, J.Q. Li, S.N. Zhu, Y.Y. Zhu, X. Zhang, Extraordinary optical transmission induced by excitation of a magnetic plasmon propagation mode in a diatomic chain of slit-hole resonators, Phys. Rev. B 79 (2009) 024304.
[39] L.P. Wang, Z.M. Zhang, Phonon-mediated magnetic polaritons in the infrared region, Opt. Express 19 (2011) A126–A135.
[40] A.V. Zayats, I.I. Smolyaninov, A.A. Maradudin, Nano-optics of surface plasmon polaritons, Phys. Rep. 408 (2005) 131–314.
[41] M.-W. Tsai, T.-H. Chuang, C.-Y. Meng, Y.-T. Chang, S.-C. Lee, High performance midinfrared narrow-band plasmonic thermal emitter, Appl. Phys. Lett. 89 (2006) 173116.
[42] Y.-H. Ye, Y.-W. Jiang, M.-W. Tsai, Y.-T. Chang, C.-Y. Chen, D.-C. Tzuang, Y.-T. Wu, S.-C. Lee, Localized surface plasmon polaritons in Ag/SiO_2/Ag plasmonic thermal emitter, Appl. Phys. Lett. 93 (2008) 033113.
[43] Y.-W. Jiang, Y.-T. Wu, M.-W. Tsai, P.-E. Chang, D.-C. Tzuang, Y.-H. Ye, S.-C. Lee, Characteristics of a waveguide mode in a trilayer Ag/SiO_2/Au plasmonic thermal emitter, Opt. Lett. 34 (2009) 3089–3091.
[44] C. Wu, B. Neuner III, G. Shvets, J. John, A. Milder, B. Zollars, S. Savoy, Large-area wide-angle spectrally selective plasmonic absorber, Phys. Rev. B 84 (2011) 075102.
[45] E.D. Palik, Handbook of Optical Constants of Solids, Academic Press, San Diego, CA, 1985.
[46] J.I. Watjen, T.J. Bright, Z.M. Zhang, C. Muratore, A.A. Voevodin, Spectral radiative properties of tungsten thin films, Int. J. Heat Mass Transfer, 2012, in press.
[47] B.J. Lee, Y.B. Chen, Z.M. Zhang, Transmission enhancement through nanoscale metallic slit arrays from the visible to mid-infrared, J. Comput. Theor. Nanosci. 5 (2008) 201–213.
[48] P. Lalanne, Improved formulation of the coupled-wave method for two-dimensional gratings, J. Opt. Soc. Am. A 14 (1997) 1592–1598.
[49] M.G. Moharam, E.B. Grann, D.A. Pommet, T.K. Gaylord, Formulation for stable and efficient implementation of the rigorous coupled-wave analysis of binary gratings, J. Opt. Soc. Am. A 12 (1995) 1068–1076.
[50] M.G. Mauk, V.M. Andreev, Gasb-related materials for tpv cells, Semicond. Sci. Technol. 18 (2003) S191.
[51] J. Zhou, E.N. Economon, T. Koschny, C.M. Soukoulis, Unifying approach to left-handed material design, Opt. Lett. 31 (2006) 3620–3622.
[52] Y. Xuan, Y. Zhang, Investigation on the physical mechanism of magnetic plasmons polaritons, J. Quant. Spectrosc. Radiat. Transfer, 2013, in press.
[53] Z. Zhang, K. Park, B.J. Lee, Surface and magnetic polaritons on two-dimensional nanoslab-aligned multilayer structure, Opt. Express 19 (2011) 16375–16389.
[54] H. Raether, Surface Plasmons on Smooth and Rough Surfaces and on Gratings, Springer-Verlag, Berlin, 1988.
[55] F. Marquier, M. Laroche, R. Carminati, J.J. Greffet, Anisotropic polarized emission of a doped silicon lamellar grating, J. Heat Transfer 129 (2007) 11–16.
[56] H.F. Ghaemi, T. Thio, D.E. Grupp, T.W. Ebbesen, H.J. Lezec, Surface plasmons enhance optical transmission through subwavelength holes, Phys. Rev. B 58 (1998) 6779–6782.
[57] Y.-B. Chen, C.-J. Chen, Interaction between the magnetic polariton and surface plasmon polariton, Opt. Commun. 297 (2013) 169–175.